Microscopic lymph node tumor burden quantified by macroscopic dual-tracer molecular imaging

Kenneth M. Tichauer[1,*], **Kimberley S. Samkoe**[2], **Jason R. Gunn**[3], **Stephen C. Kanick**[3], **P. Jack Hoopes**[2,3], **Richard J. Barth**[2], **Peter A. Kaufman**[4], **Tayyaba Hasan**[5], and **Brian W. Pogue**[2,3,5,*]

[1]Biomedical Engineering, Illinois Institute of Technology, Chicago, IL 60616

[2]Department of Surgery, Geisel School of Medicine, Hanover, NH 03755

[3]Thayer School of Engineering, Dartmouth College, Hanover, NH 03755

[4]Department of Medicine, Geisel School of Medicine, Lebanon, NH 03756

[5]Wellman Center for Photomedicine, Massachusetts General Hospital, Boston, MA 02114

Abstract

Lymph node biopsy (LNB) is employed in many cancer surgeries to identify metastatic disease and stage the cancer, yet morbidity and diagnostic delays associated with LNB could be avoided if non-invasive imaging of nodal involvement was reliable. Molecular imaging has potential in this regard; however, variable delivery and nonspecific uptake of imaging tracers has made conventional approaches ineffective clinically. A method of correcting for non-specific uptake with injection of a second untargeted tracer is presented, allowing tumor burden in lymph nodes to be quantified. The approach was confirmed in an athymic mouse model of metastatic human breast cancer targeting epidermal growth factor receptor, a cell surface receptor overexpressed by many cancers. A significant correlation was observed between *in vivo* (dual-tracer) and *ex vivo* measures of tumor burden ($r = 0.97$, $p < 0.01$), with an ultimate sensitivity of approximately 200 cells (potentially more sensitive than conventional LNB).

Keywords

fluorescence; metastasis; surgical oncology; tracer kinetics; mouse xenograft; breast cancer

---

*Corresponding Author: Brian W. Pogue, Thayer School of Engineering, Dartmouth College, 14 Engineering Drive, Hanover, NH 03755, 1-603-646-3861, brian.w.pogue@dartmouth.edu or Kenneth M. Tichauer, Biomedical Engineering, Illinois Institute of Technology, Chicago, IL 60616, 1-312-567-3858, ktichaue@iit.edu.

Introduction

A non-invasive method to measure the extent of cancer spread to tumor draining lymph nodes is presented. The presence or absence of cancer in tumor-draining lymph nodes is recognized as a key element for staging many cancers, and as a result, node localization and biopsy have become standards of care during, most notably for breast cancer and cutaneous melanoma.[1] Notwithstanding its importance in staging cancer,[2] lymph node dissections can be associated with overtreatment and significant morbidity (*e.g.*, surgical nerve damage and post-surgical lymphedema),[3] and histological analysis of lymph nodes can be time-consuming, delaying subsequent procedures. Motivated by these deficiencies in conventional biopsy, many have attempted to estimate tumor burden non-invasively in animal models and clinical studies, typically employing molecular imaging of cancer-targeted imaging tracers, a comprehensive review of which was provided by Sampath *et al*.[4] While these groups have demonstrated promising results, over thirty years of effort in this area, and at least ten antibody-based imaging tracer clinical trials in the 1980s and 1990s, has failed to result in any widespread use of targeted imaging tracers to detect lymph node metastases. Many factors may affect the success of such approaches, but it is thought that high interstitial variability in tracer delivery to lymph nodes and nonspecific tracer uptake in healthy nodes are the major problems obfuscating the ability to relate tracer uptake directly to tumor burden [5].

One proposed method to account for variability in tracer delivery has been the simultaneous injection of a second "untargeted" tracer that can be used to account for binding-independent characteristics of a targeted tracer's uptake.[6–8] Our group has recently advanced these dual-tracer approaches to quantify cell-surface cancer receptor concentrations in primary tumors using planar fluorescence imaging[9] and fluorescence tomography.[10] Here, these principles were adapted to lymph imaging and evaluated in a mouse model of breast cancer metastasis. We used an epidermal growth factor receptor (EGFR)-specific antibody labeled with a near-infrared fluorophore as the targeted tracer, and an isotype control antibody labeled with a different near-infrared fluorophore as the untargeted tracer.

Results

In total, we imaged and analyzed tumor burden in the left and right axillary lymph nodes of twenty-two mice (18 tumor-bearing mice and 4 controls). Six additional tumor-bearing mice had to be sacrificed owing to complications with primary tumor resection surgery. Bioluminescence imaging of tumor spread to lymph nodes was only detectable in 5 of 36 lymph nodes imaged, corresponding to the largest levels of tumor burden (greater than 2,000 cells). Bioluminescence and corresponding hemotoxylin and eosin histological staining was used to verify tumor metastasis to the lymph nodes (Fig. 1b,e). We observed metastases in both the right and left axillary lymph nodes. Thirteen of the tumor-bearing mice had more than 200 tumor cells in either or both the right or left axillary lymph node measured by qPCR (6 on only the right, 4 on only the left, and 3 in both). We focused on the 200-tumor-cell threshold, as it was two standard deviations above the detection limit of the qPCR approach: 100 ± 50 cells.

We were unable to identify the affected side of the tumor-bearing mice from 3-h fluorescence uptake images of either the targeted or untargeted tracers on their own in any of the tumor-bearing mice (Fig. 2). In fact, there were no observable differences amongst fluorescence uptake in the control and tumor-bearing groups (Fig. 3c,d). However, once the lymph node molecular concentration imaging (LN-MCI) algorithm was applied to the tracer uptake curves, the resultant images of EGFR concentration could be used to clearly identify the affected side of the mouse, demonstrating little appreciable EGFR expression in controls.

In all control animal lymph nodes, the average targeted tracer uptake was not significantly different from the average untargeted tracer uptake at any time point ($p > 0.05$). Conversely, targeted tracer retention was significantly higher than untargeted tracer retention in tumor-bearing lymph nodes ($p < 0.001$). The quantification of this difference through the LN-MCI approach at multiple time points following tracer injection with the ratio, (targeted tracer – untargeted tracer)/untargeted tracer, demonstrated an obvious correlation with the extent of tumor burden by 3 h post-injection presented in (Fig. 3a). The time it took for this ratio to stabilize was inversely correlated with the measured lymph flow (Fig. 3b) – see Online Methods.

Observing targeted fluorescence uptake alone, we observed very high variability in the efficiency of tracer delivery from the site of injection to the axillary lymph nodes, with an average targeted fluorescence of 0.1 ± 0.1 at 3 h (range: $0.03 - 0.18$). No appreciable or statistical ($p > 0.05$) differences were observed amongst any of the lymph node groups: controls, < 200 cells, and > 200 cells (Fig. 3c). When the same boxplot analysis was applied to the average EGFR concentration in each lymph node determined by the LN-MCI algorithm (Fig. 3e,f), lymph nodes with greater than 200 tumor cells identified by qPCR were observed to have a significantly higher EGFR concentration than both the control group and the < 200 cells group ($p < 0.05$), with an average EGFR concentration of 1.6 ± 1.0 nM, compared to 0.008 ± 0.005 nM and 0.02 ± 0.02 nM for the control and < 200 cell groups, respectively. No statistically significant difference was observed between controls and the < 200 cell group with Bonferroni correction and a two-tailed analysis ($p > 0.05$); however, further investigations may yield significance since we observed $p < 0.05$ in a simple one-tailed t-test.

In addition to these findings, we observed a statistically significant correlation ($r = 0.97$, $p < 0.01$) between the level of EGFR concentration measured and the number of cells detected (Fig. 4). The slope of this correlation was 0.4 pM cell^{-1} cm^{-2}. By including results from all lymph nodes excised from tumor-bearing mice, there remained a statistically significant correlation between *in vivo* measured EGFR concentration and qPCR detected cell number ($r = 0.97$, $p < 0.01$). To determine if the correlation observed between measured EGFR concentration and tumor cell burden in lymph nodes had a physiological basis, flow cytometry[9] was employed to determine the average number of EGFRs per cell: $1.5 \times 10^5 \pm 0.2 \times 10^5$. An additional flow cytometry analysis of healthy lymph node cells showed no inherent EGFR expression, with a value of $10 \pm 2,000$ receptors per cell.

For a simulated targeted concentration of 1 nM, the average estimated target concentration was 0.14 ± 0.08, 0.52 ± 0.04, 0.84 ± 0.04, and 0.95 ± 0.04 measured with the LN-MCI model (**Online Methods** Eq. 4) when employed at 20, 60, 120, and 180 min post tracer injection, respectively (Fig. 5c,d).

Discussion

The novelty of the lymph node, molecular concentration imaging (LN-MCI) approach lies in the use of a second, "untargeted" tracer to account for non-specific uptake of a cancer-targeted imaging tracer. We demonstrated that the approach was capable of quantifying targeted molecule concentrations, as a surrogate of tumor burden, without requiring the tracer uptake images on their own to be quantitative. The approach has the potential to be applied for any cell-surface cancer cell receptor targeted imaging agent using any molecular imaging modality (or combination of modalities), allowing for simultaneous monitoring of more than one tracer. In the present study, we explored the potential of this LN-MCI approach for imaging epidermal growth factor receptor (EGFR) using planar fluorescence imaging, comparing the results to *ex vivo* qPCR measurements of axillary lymph node tumor burden.

Though any cancer cell marker could be targeted with LN-MCI, EGFR was chosen in here because 1) antibodies for EGFR are already in clinical use, which could improve the potential for clinical approval of imaging agent conjugated forms;[11] 2) it is overexpressed in many cancer types;[12] and 3) there is a high concordance between EGFR expression in primary tumor and lymph node metastases in a number of cancer types,[13–19] so that conventional biopsy of the primary tumor could confirm whether or not EGFR was a suitable target. A potential drawback of targeting EGFR is that it is expressed in a number of other healthy human tissues such as skin.[20] This could result in substantial background signal if the tracers were injected systemically; however, the localized injection approaches used in lymph node tracking result in the majority of tracer remaining in the lymph system.[21] This study demonstrated a similar finding, with at least 10 times greater measured fluorescence from the axillary lymph nodes than from surrounding healthy skin at all time points in all mice. Therefore, background EGFR binding could be considered negligible when translating this approach to the clinic, simply because the delivery of the imaging agent to the tissue surrounding the lymph node would be negligible.

The salient findings of this study were: 1) axillary lymph node concentrations of EGFR estimated by the LN-MCI model demonstrated a statistically significant correlation with *ex vivo* measures of lymph node tumor burden (slope = 0.4 pM cell^{-1} cm^{-2}, $p < 0.01$) by 3 h post-tracer-injection; and 2) the ultimate sensitivity of the LN-MCI approach and the *ex vivo* qPCR method of quantifying lymph node tumor was approximately 200 cells. The 3 h delay before the LN-MCI approach became accurate was supported by the simulation studies attributable to the fact that it takes time for a significant proportion of signal to come from bound tracer, the length of which was inversely proportional to the lymph flow rate (Fig. 3b and 5d).

With respect to the first finding, the slope of the correlation at 0.4 pM cell^{-1} cm^{-2} matched well with a theoretical slope of 0.6 pM cell^{-1} cm^{-2} assuming 1.5×10^6 EGFRs per cell within a 2 mm diameter lymph node. Recently, Brader *et al*. demonstrated a weak correlation between uptake of a targeted positron emission tomography tracer and lymph node weight[22] and Tafreshi *et al*. demonstrated a correlation between targeted fluorophore uptake and the number of cancer cells directly injected into an axillary lymph node.[23,24] Though exciting, each of these approaches utilizes a single imaging tracer and could be prone to problems with nonspecific uptake, tracer delivery rate, and signal quantification in clinical applications, particularly if physicians prefer to inject the tracers interstitially as is done currently with lymph node localization in blue-dye imaging and lymphoscintigraphy.[1] To account for delivery variability, a ratiometric approach was demonstrated by Savariar *et al*. using a single dual-fluorescence peptide that experiences a change in fluorescent ratio upon cleavage by tumor associated matrix metalloproteinases-2 and -9.[25] The approach was found to offer substantial improvements in the detection of lymph node metastases despite considerable nonspecific uptake of the tracer in surrounding tissues, similar to the results in the current study. One advantage of our approach is the ability to estimate the extent of tumor burden, rather than just the presence of tumor. Since the activation of specific ratiometric peptide in Savariar *et al.* is irreversible, the ratio at any given time point will be dynamically related to the MMP-2,9 concentration, making it difficult to isolate MMP-2,9 concentration without multiple time point kinetics. Furthermore, kinetics of the cleaved fluorophore moving through the different compartments of the tissue would also have to be accounted for. However, the ability for a dual-labeled activatable tracer to act as both a targeted and untargeted imaging agent could have benefits for clinical translation of MCI approaches and efforts are ongoing in this area. In lymph node mapping, dual-tracer imaging may offer a road to faster clinical translation, as in may nodal resection surgeries an untargeted imaging agent in the form of a blue dye is already used commonly to locate the nodes and applications that employ this dye as an untargeted tracer are underway.

The 200-cell sensitivity observed in this study suggests a higher sensitivity than current invasive biopsy approaches. Histopathology can detect single tumor cells; however, it would be too time-consuming to microscopically evaluate an entire lymph node. The current method of lymph node analysis is to slice the lymph node into 2-mm thick slices, imaging the surface of each so as not to miss any macrometastases, which have been arbitrarily defined as clusters of tumor cells exceeding 2 mm in diameter.[26] Micrometastases (0.2 – 2 mm diameter) and isolated tumor cell clusters (ITCs: < 0.2 mm diameter) can be seen in lymph node sections if they overlap the region where the lymph node was cut; however, they will not be observed if they are located outside this region.

All experiments in this study were carried out in a light-tight imaging system. Our group has recently constructed and validated a multi-wavelength imaging system capable of imaging with room lights on by taking advantage of pulsed fluorescence excitation and time-gated detection, which an pave the way to a more rapid clinical translation of the finding in this study.[27]

To correlate with lymph node tumor burden, LN-MCI requires four suppositions to be true: 1) the targeted and untargeted tracers have equivalent delivery to the lymph node; 2) the

targeted tracer concentration is negligible compared to the concentration of the targeted receptor; 3) the metastatic cancer cells overexpress the receptor being targeted; and 4) the imaging approach needs to be able to detect fluorescence in the lymph node of interest.

With respect to 1), the relative equivalency of the tracer uptake curves in tumor-free axillary lymph nodes (Fig. 3c) suggests similar lymph uptake, flow kinetics, pharmacokinetics, biodistribution, and photostability for the two tracers employed, and similar negligible autofluorescence and optical properties between the two imaging channels within the 3 h imaging window. The equivalency of tracer delivery and washout to the lymph node was expected since these parameters are primarily dependent on size,[28] and both tracers were based on ~150 kDa antibodies, labeled with ~1 kDa fluorphores. There was a slight bias with the average EGFR estimate in control nodes of 0.2 ± 0.2 nM, which could have been a result of background EGFR binding or a slight difference in tracer delivery rate; however, this did not affect the apparent 200 cell sensitivity of the LN-MCI approach. Every new set of tracers should be tested before being used in this dual-tracer imaging approach and novel dual-fluorescence ratiometric tracers may represent the best way forward.[25]

With respect to 2): for the current study, assuming the cells are roughly 20 μm in diameter, then in the volume surrounding the cell (~4,000 μm^3, assuming the cell to be a sphere), there are on average 1.5×10^6 EGFR molecules yielding a localized EGFR concentration of ~ 60 nM. Extrapolating from the average fluorescence at the site of injection over time (Fig. 5b), and assuming all of the fluorescence not in the footpad had accumulated in the lymph node, then approximately 0.1% of the injected dose of 0.05 nanomoles at a maximum could be in the axillary lymph node. If the internal diameter of the lymph node is assumed to be about 2 mm, and the tracer is homogeneously distributed throughout the lymph node, this results in a maximum concentration of targeted tracer of ~ 6 nM, about 10% of the localized EGFR concentration. Moreover, since tracer is constantly flowing out the lymph node and not all of the tracer will have traveled through the axillary lymph node, the actual concentration of tracer in the lymph node was likely at least an order of magnitude less.

With respect to 3), gene expression can vary from patient to patient and even within a tumor.[29] Therefore, the optimal receptor to target will be different from patient to patient, the determination of which may require novel approaches. New high-throughput circulating-tumor-cell gene analysis approaches may be one such way of determining the optimal target.[30]

Finally, with respect to 4): the limited depth sensitivity of the planar fluorescence imaging presented in this study (~1.5–2 mm determined by the Monte Carlo Simulations for both targeted and untargeted imaging agents when assuming homogeneous distribution of fluorescence) would not prevent its use intraoperatively in the clinic; however, more non-invasive applications could be achieved using fluorescence tomography approaches with larger source-detector spacing.[31] These approaches are typically associated with poorer spatial resolution, that could be improved using anatomical imaging guidance: for example ultrasound-guided fluorescence tomography has been shown to provide sensitivity to optical properties at considerable depths (1–4 cm) in breast tissue.[32,33] The anatomical guidance could also be used to avoid analysis of signals arising from tissue surrounding the lymph

nodes that could be impacted by background EGFR binding.[20] Depth sensitivity beyond a few centimeters will likely require nuclear medicine approaches such as dual-energy single photon emission tomography[34] in order to image both targeted and untargeted imaging agents simultaneously. This could be ideal, since SPECT tracers and gamma cameras are widely used to locate lymph nodes through lymphoscintigraphy and the principles demonstrated in the current paper could be readily adapted to such deeper depth sensitivity approaches.

Online Methods

Breast cancer lymph metastasis model

All animal procedures were carried out in accordance with the Institutional Animal Care and Use Committee at Dartmouth College under an approved protocol. To evaluate the potential of the lymph node RCI model to be used to detect tumor burden in tumor-draining lymph nodes, a mouse model of lymph node metastasis that was as realistic as possible was studied. In all, 28 6-to-8-week-old athymic nude female mice (Crl:NU(NCr)-Foxn1[nu], Charles River Laboratories, Wilmington, MA) were used in the experiment. 1×10^6 MDA-MB-231-luc-D3H2LN human breast cancer cells (PerkinElmer, Waltham, MA) were injected into the right inferior mammary fat pad of twenty-four of the mice with four mice randomly selected as controls with no tumor injection. The cells were purchased expressly for this study, confirmed to be pathogen free from the supplier by the IMPACT Profile I (PCR) at the University of Missouri Research Animal Diagnostic and Investigative Laboratory. The number of mice were chosen based on a sample size estimation on the correlation between the imaging method of tumor burden estimation and *ex vivo* analyses of tumor burden, in addition to a 30% attrition rate owing to complications of tumor surgery. The calculation assumed a probability of Type I Error of 0.05, a Power = 0.9, and a correlation coefficient of 0.8. The primary tumors were allowed to grow for 6 weeks before the primary tumors were surgically removed at a size of 2.4 ± 1.1 cm^3. The mice were then returned to their cages for a further 12 weeks to allow metastases time to form prior to imaging.[35] Select mice were imaged earlier if primary tumor grew back to a size of 10% of the mass of the mouse. The MDA-MB-231-luc-D3H2LN was chosen for a number of reasons: 1) the cell line has been specifically selected from lymph node metastases and therefore has a high likelihood of spreading to the axillary lymph node; 2) the cells have been transfected with a luciferase gene, which can be used to make the cells bioluminesce with injection of luciferin[36] providing a means of monitoring metastatic tumor growth; and 3) the cells moderately overexpress the cell membrane receptor, epidermal growth factor receptor (EGFR)[37], a receptor overexpressed in many cancer types[12], and targeted in this study.

Fluorescence imaging

Four weeks following the surgical removal of the primary tumor, the mice were anesthetized with 1.5–2% isofluorane and placed in a supine position with forelegs taped above their heads to expose the axillary lymph nodes (Fig. 1a) on the heated (37 °C) bed of a Pearl Imaging System (LICOR Biosciences, Lincoln, NE), a commercial small animal planar fluorescence imaging system with white-light and two fluorescent imaging channels: a "700 nm channel" and an "800 nm channel". The system is based on wide-field illumination and

detection using "stadium" lighting for illumination and a 22-bit charge-coupled device camera for detection, providing 83-μm resolution at the focal plane. The 700 channel excites fluorescence around 685 nm with an intensity distribution of 2 mW cm^{-2} and detects emission about 720 nm, while the 800 channel excites fluorescence around 785 nm with an intensity distribution of 4 mW cm^{-2} and detects about 820 nm. To capitalize on the wavelength bands of the Pearl's two fluorescent channels for carrying out dual-tracer EGFR concentration imaging, an EGFR-specific antibody was labeled with IRDye-800CW to act as a targeted tracer, and an untargeted antibody was labeled with IRDye-700DX to act as the untargeted tracer (see *Fluorescence tracer synthesis* Section). Both tracers are known to demonstrate strong photostability at the excitation intensities employed by the Pearl Imaging System.[38] Once positioned in the Pearl, white light, 700 nm channel, and 800 nm channel images were acquired prior to injecting 0.1 nanomoles of each tracer simultaneously intradermally into each front footpad. The front footpad of the mice was chosen as a site of injection since it has been shown previously that injections carried here are preferentially drained through the axillary lymph nodes, a superficial node in mice that is easy to image.[39] Following tracer injection, all three image types were collected sequentially (each image type having a duration of approximately 5 s) at 2-min intervals up to 3 h post-injection, at which point the mice were euthanized and the right and left axillary lymph nodes were excised and analyzed with quantitative real-time PCR for an *ex vivo* estimate of tumor burden. Temporal images of targeted and untargeted tracers were analyzed with in-house software written in the programming language Matlab (MathWorks, Natick, MA) to apply the dual-tracer RCI algorithm on a pixel-by-pixel basis and calculate a parametric map of EGFR concentration. The average concentration of EGFR in each axillary lymph node, to be used as a surrogate of tumor burden, was calculated from a 5-mm circular region-of-interest centered on each lymph node (Fig. 1c). The size of the region-of-interest was chosen based on the largest lymph node measured *ex vivo* so as not to miss any signal arising from any lymph node.

Quantitative PCR for tumor burden validation

Since a human breast cancer cell line was grown in a mouse model in this study, it was possible to use genetic markers to determine the ratio of cancer to normal tissue with real-time PCR based on established approaches.[40,41] For improved sensitivity in this regard, the presence of luciferase gene expression was analyzed instead of a human specific gene, since the luciferase gene in not expressed naturally by mice but was transfected into the MDA-MB-231-luc-D3H2LN cell line by the manufacturer. Total RNA was isolated from flash frozen lymph nodes using RNeasy mini kit and Qiashredder (Qiagen, Venlo, Netherlands), and 18-gauge needles to homogenize the tissue. To assess gene expression levels, cDNA was prepared from lymph node RNA using the Superscript III First Strand cDNA Synthesis Kit and oligo dT primers (Life Technologies, Grand Island, NY). Reactions (25 μl) were set up using 2X iQ Supermix (Biorad, Hercules, CA), pre-validated Luciferase primer and probe set (Assays on Demand, Applied Biosystems, Life Technologies), and equivalent amounts of template cDNA. Quantitative real-time PCR was performed with a Biorad CFX96 Real-Time PCR Detection System (Biorad). Each sample was assayed in duplicate, and 18s rRNA served as the endogenous control for normalization. The expression levels for each gene were calculated relative to a standard curve of known tumor cells added to naïve

lymph nodes. For the standard curve, 10, 100, 1,000, 10,000, and 100,000 were added in quadruplicate (Fig. 1f). All procedures and analyses were carried out blinded to the fluorescent imaging results by author JRG.

Fluorescence tracer synthesis

The labeling procedures for the targeted and untargeted tracers were essentially the same. The EGFR-specific antibody, Erbitux (clinical grade from Bristol_Myers Squibb, Princton, NJ) was labeled with the NHS ester form of IRDye-800CW (LICOR Biosciences), and mouse IgG (Athens Research and Technology, Athens, GA), an untargeted isotype control of Erbitux was labeled with the NHS ester form of IRDye-700DX (LICOR Biosciences). The antibodies were initially diluted in phosphate buffer solution (PBS) before being run through a 5-ml polyacrylamide desalting column to remove sodium azide. With the antibodies in 500-μl aliquots, 50 μl of 1 M sodium bicarbonate solution was added to increase the pH of the solution for optimal binding to the fluorophore as per manufacturer instructions. The fluorophores were diluted in DMSO and added to the antibody aliquots in a 3:1 dye-to-antibody ratio. These solutions were then left to mix on a magnetic stir plate for 2 h at room temperature. The dye-antibody conjugates were then separated from unassociated antibody and fluorophore with a desalting column using PBS to flush. Presence of the conjugate was confirmed in the resulting aliquots with a fluorimeter and then concentrated with a 50 kDa MW Vivaspin 2 (GE Healthcare).

Flow cytometry

The number of EGFRs per cell of the MDA-MB-231-luc-D3H2LN line and healthy lymph node tissue was quantified by flow cytometry. For MDA-MB-231-luc-D3H2LN, cells were grown in vitro until they reached a confluence of 80%, they were then trypsinized, counted, and washed with PBS. Three sets of 5×10^5 cells were then labeled with 4 μg ml^{-1} of EGF Biotin (Molecular Probes, Invitrogen, Camarillo, CA), washed, and secondarily labeled with a 1:25 dilution of Cy5-Streptavidin (Invitrogen, Camarillo, CA). Three additional sets of 5×10^5 cells were stained only with the 1:25 dilution of Cy5-Streptavidin to account as controls to account for autofluorescence and non-specific staining. Each set of cells was load sequentially into a flow cytometer (FACSCalibur), and data were acquired with Cell Quest Acquisition software (Becton Dickinson, San Jose, CA). In addition, a calibration standard was run using Quantum Cy5 MESF beads as described by the manufacturer (Bangs Laboratory, Fishers, IN) to quantify EGFR expression.[9] To analyze the expression of EGFR in healthy mouse lymph node cells, axillary lymph nodes of three mice were dissected upon sacrifice. They were then placed between two general-purpose glass microscope slides, physically minced in order to release the cells, and put into tissue culture media. These solutions were then spun down and three sets of 5×10^5 cells were selected for flow cytometry analysis as discussed above. All analyses were repeated in triplicate on three different days and the lymph nodes were taken from three different control mice that were not used in this imaging study. All procedures and analyses were carried out blinded to the group by author JRG.

Lymph node molecular concentration imaging

The lymph node molecular concentration imaging (LN-MCI) approach is based on dual-tracer compartmental modeling that has been described for imaging primary cancer receptor concentrations in detail previously.[9,10,42–47] To adapt the original RCI approach for detecting metastatic cells in the lymph system, slightly modified compartment models were developed for the targeted and untargeted tracer uptakes (Fig. 5a). Within the lymph node, the targeted tracer was modeled to be freely associated (C_f) or bound to targeted tumor cell receptors (C_b), and the whole system was modeled to be driven by the concentration of tracer in the upstream lymphatic vessels, C_l, which enters the lymph node at flow rate, F_l. The targeted tracer was modeled to only be able to exit the lymph node into the downstream lymphatics at the same flow rate, F_l, assuming flow equilibrium conditions. Rate-constants k_3 and k_4 were used to describe the rate of tracer-receptor association and dissociation, respectively. By assuming: 1) the unbound (freely-associated) concentration of tracer in the lymph node is always homogeneously distributed, and 2) the concentration of targeted tracer in the lymph node is negligible compared to the concentration of targeted receptor, a system of first-order differential equations can be developed to govern the rate of change of tracer concentration in each compartment. For the targeted tracer:

$$\frac{dC_f(t)}{dt} = F_l C_i(t) - F_l C_f(t) - k_3 C_f(t) + k_4 C_b(t),$$
$$\frac{dC_b(t)}{dt} = k_3 C_f(t) - k_4 C_b(t), \text{ and} \tag{1}$$
$$ROI_T(t) = \eta_T \left[C_f(t) + C_b(t) \right],$$

where $ROI_T(t)$ represents the measured fluorescence signal from the uptake of the targeted tracer in the lymph node as a function of time, t, and the parameter η_T represents the detection efficiency of the imaging system for the targeted tracer. For the untargeted tracer:

$$\frac{dC_U(t)}{dt} = F_l C_i(t) - F_l C_U(t) \text{ and}$$
$$ROI_U(t) = \eta_U C_U(t), \tag{2}$$

where $C_U(t)$ is the concentration of untargeted tracer in the lymph node, $ROI_U(t)$ represents the measured fluorescence signal from the uptake of the untargeted tracer in the lymph node as a function of time, and the parameter η_U represents the detection efficiency of the imaging system for the untargeted tracer. The compartment model used for the untargeted tracer (Fig. 5a) was very similar to that of the targeted tracer with the exception that there was no "bound" compartment. The utility of measuring the uptake of the untargeted tracer can be plainly seen in the set of equations (1) and (2), since its uptake can be used as a surrogate of C_l, the upstream lymph vessel concentration of tracer, which is problematic/impractical to measure. From the last expressions in Eqs. (1) and (2), the following expression can be derived:[47]

$$\frac{\frac{\eta_U}{\eta_T} ROI_T(t) - ROI_U(t)}{ROI_U(t)} = \frac{C_f(t) + C_b(t) - C_U(t)}{C_U(t)}, \tag{3}$$

for any time point, t. Eq. (4), which amounts to normalizing a targeted tracer uptake image, subtracting from it an untargeted tracer uptake image, and dividing that difference by the

untargeted tracer uptake image, can be shown to be proportional to the receptor concentration if the free concentrations of the targeted and untargeted tracers share roughly the same time course [i.e., if $C_f(t) \approx C_U(t)$, and assuming that binding is an adiabatic process i.e., th at $C_b(t)/C_f(t)$ remains a constant,[48] as follows:

$$\frac{\frac{\eta_U}{\eta_T}ROI_T(t) - ROI_U(t)}{ROI_U(t)} = \frac{C_b(t)}{C_f(t)} = \frac{k_3}{k_4} \equiv BP. \quad (4)$$

The "binding potential", $BP = k_3/k_4$, is the main parameter of interest in this model because it is directly proportional to, by the tracer-receptor affinity (a parameter that can be measured *ex vivo*).[49] Equation (4) was used to estimate receptor concentration in simulations and in all animal experiments at multiple time-points up to the 3 h imaging window in this study. The ratio of detection efficiencies, η_U/η_T, was estimated by placing the stock solution of targeted and untargeted fluorescence that was injected into the mice into the Pearl Imaging and measuring the fluorescence at both wavelengths, wherein:

$$\frac{\eta_U}{\eta_T} = \frac{\Phi_U}{\Phi_T}, \quad (5)$$

if the optical properties of the tissues imaged are not significantly different between wavelengths, which is approximately true for 700 and 800 nm in biological tissue[50] – where Φ_U and Φ_T are equal to the untargeted and targeted tracer fluorescence measured from the stock solution, respectively. All image analyses were carried out blinded to the group and *ex vivo* analyses of tumor burden by author KMT.

Time-to-plateau of *BP* estimation

The ratiometric estimate of BP presented in Eq. (4) requires the ratio of bound to free concentrations of the tracer to reach a quasi-steady-state in order to be accurate, and therefore the plot of Eq. (4) over time must reach a plateau before Eq. (4) is accurate. To determine the time-to-plateau of these temporal ratiometric curves, the curves were fit with a 5th order polynomial to smooth out noise and the time-to-plateau was taken as the point the derivative of this fitted polynomial reached zero.

Lymph flow estimation

The set of differential equations in Eq. (1) and (2) can be solved in a more rigorous sense than in Eq. (4) if the temporal uptakes of ROI_T and ROI_U are assumed to be known, into a workable linear solution that precludes the need to measure C_l:[51]

$$ROI_T(t) = -\frac{F_l}{1+BP}\int_0^t ROI_T(u)\,du + \frac{\eta_U}{\eta_T}F_l\int_o^t ROI_U(u)\,du + \frac{\eta_U}{\eta_T}ROI_U(t). \quad (6)$$

Equation (6) could be used on its own to estimate F_l, η_U/η_T, and BP, respectively, with knowledge of $ROI_T(t)$ and $ROI_U(t)$ using linear least squares. In fact, initial tests have demonstrated a strong correlation between the BP estimated with Eq. (4) and that with Eq.

(6). The problem is that this approach requires continuous measurement of tracer uptake in lymph nodes and therefore may be difficult to employ clinically. In this experiment, however, tracer uptake was measured over time, allowing the lymph flow, F_l, to be estimated on a case-by-case basis. A quick unit analysis can show that the units of F_l need to be in inverse time. Conventionally, flow is measured in volume of fluid flowing through a volume of tissue per time (*e.g.*, mL lymph fluid mL tissue^{-1} min^{-1}). In this study, the units were simplified to min^{-1} for simplicity.

Noise analysis

Theoretical targeted and untargeted tracer uptake curves in a tumor-bearing lymph node were created using full analytical solutions to the system of expressions in Eq. (1)[52] and Eq. (2)[53], respectively. To carry this out, the lymph input function, C_l, was estimated by the derivative of the fluorescence measured in footpad site of injection on the mice in the animal experiment (Fig. 5b), assuming that all fluorescence leaving the site of injection travels through the lymph system and passes through the lymph node of interest. For the targeted tracer, k_4 was assumed to be 0.06 min^{-1} from literature values,[54] and k_3 was estimated to be 0.16 min^{-1}, assuming a target concentration of 1 nM, which was a typical level found in mouse experiments, with a tracer affinity of 2.6 nM^{-1} [affinity of Erbitux for EGFR][54]. All simulations were repeated over a range of lymph flow rates, F_l, 0.05 – 0.25 min^{-1}, determined from the range of lymph node flow rates measured in the mouse experiments (average $F_l = 0.15 \pm 0.07$ min^{-1}) by fitting the analytical solution to Eq. (2)[53] to the untargeted tracer lymph node uptake. 2% random Gaussian noise was added to all simulated curves. The resulting curves were then fit with the models in Eq. 3 and Eq. 4 using in-house software written in MATLAB (Mathworks, Natick, MA) to evaluated the noise sensitivity and accuracy of each model. Noise addition was repeated 1×10^5 times.

Statistical Analysis

All statistics in this study were carried out with the statistical package SPSS (IBM®, Armonk, NY). A one-way ANOVA was used to compare means between tumor-burden groups (control, < 200 cells, > 200 cells) to compare targeted tracer fluorescence uptake and measured EGFR concentration in each group. Variance equivalency between groups was determined by a Levene Statistic: if $p > 0.05$ variance was assumed equivalent, whereas if $p < 0.05$, variance was not assumed equivalent. Bonferroni correction was employed to account for multiple comparisons in equivalent variance data sets, whereas for nonequivalent variance, Tamhane correction was employed. Linear regression was employed to compare *in vivo* EGFR concentration with *ex vivo* qPCR evaluations of tumor cell burden. Statistical significance was based on a two-tailed $p < 0.05$ with equal variance assumed unless stated otherwise. All data are presented as mean ± s.d.

Acknowledgments

References

1. Chen SL, Iddings DM, Scheri RP, Bilchik AJ. Lymphatic mapping and sentinel node analysis: current concepts and applications. CA: a cancer journal for clinicians. 2006; 56:292–309. quiz 316–297. [PubMed: 17005598]

2. Tobler NE, Detmar M. Tumor and lymph node lymphangiogenesis--impact on cancer metastasis. Journal of leukocyte biology. 2006; 80:691–696. [PubMed: 16793912]

3. Schrenk P, Rieger R, Shamiyeh A, Wayand W. Morbidity following sentinel lymph node biopsy versus axillary lymph node dissection for patients with breast carcinoma. Cancer. 2000; 88:608–614. [PubMed: 10649254]

4. Sampath L, Wang W, Sevick-Muraca EM. Near infrared fluorescent optical imaging for nodal staging. Journal of biomedical optics. 2008; 13:041312. [PubMed: 19021320]

5. Reilly RM, et al. Problems of delivery of monoclonal antibodies. Pharmaceutical and pharmacokinetic solutions. Clinical pharmacokinetics. 1995; 28:126–142. [PubMed: 7736688]

6. Liu JT, et al. Quantifying cell-surface biomarker expression in thick tissues with ratiometric three-dimensional microscopy. Biophysical journal. 2009; 96:2405–2414. [PubMed: 19289065]

7. Pogue BW, et al. Imaging targeted-agent binding in vivo with two probes. Journal of biomedical optics. 2010; 15:030513. [PubMed: 20614996]

8. Baeten J, Haller J, Shih H, Ntziachristos V. In vivo investigation of breast cancer progression by use of an internal control. Neoplasia. 2009; 11:220–227. [PubMed: 19242603]

9. Tichauer KM, et al. In vivo quantification of tumor receptor binding potential with dual-reporter molecular imaging. Molecular imaging and biology : MIB : the official publication of the Academy of Molecular Imaging. 2012; 14:584–592. [PubMed: 22203241]

10. Davis SC, et al. Dynamic dual-tracer MRI-guided fluorescence tomography to quantify receptor density in vivo. Proceedings of the National Academy of Sciences of the United States of America. 2013; 110:9025–9030. [PubMed: 23671066]

11. Saltz LB, et al. Phase II trial of cetuximab in patients with refractory colorectal cancer that expresses the epidermal growth factor receptor. Journal of clinical oncology : official journal of the American Society of Clinical Oncology. 2004; 22:1201–1208. [PubMed: 14993230]

12. Nicholson RI, Gee JM, Harper ME. EGFR and cancer prognosis. European journal of cancer. 2001; 37 (Suppl 4):S9–15. [PubMed: 11597399]

13. van Agthoven T, Timmermans M, Dorssers LC, Henzen-Logmans SC. Expression of estrogen, progesterone and epidermal growth factor receptors in primary and metastatic breast cancer. International journal of cancer. Journal international du cancer. 1995; 63:790–793. [PubMed: 8847135]

14. Wei Q, et al. EGFR, HER2, and HER3 expression in laryngeal primary tumors and corresponding metastases. Annals of surgical oncology. 2008; 15:1193–1201. [PubMed: 18172732]

15. Wei Q, et al. EGFR, HER2 and HER3 expression in esophageal primary tumours and corresponding metastases. International journal of oncology. 2007; 31:493–499. [PubMed: 17671674]

16. Shen L, et al. EGFR and HER2 expression in primary cervical cancers and corresponding lymph node metastases: implications for targeted radiotherapy. BMC cancer. 2008; 8:232. [PubMed: 18700025]

17. Carlsson J, Shen L, Xiang J, Xu J, Wei Q. Tendencies for higher co-expression of EGFR and HER2 and downregulation of HER3 in prostate cancer lymph node metastases compared with corresponding primary tumors. Oncology letters. 2013; 5:208–214. [PubMed: 23255921]

18. Bue P, et al. Expression of epidermal growth factor receptor in urinary bladder cancer metastases. International journal of cancer. Journal international du cancer. 1998; 76:189–193. [PubMed: 9537579]

19. Italiano A, et al. Epidermal growth factor receptor (EGFR) status in primary colorectal tumors correlates with EGFR expression in related metastatic sites: biological and clinical implications. Annals of oncology : official journal of the European Society for Medical Oncology / ESMO. 2005; 16:1503–1507. [PubMed: 15980160]

20. Real FX, et al. Expression of epidermal growth factor receptor in human cultured cells and tissues: relationship to cell lineage and stage of differentiation. Cancer research. 1986; 46:4726–4731. [PubMed: 3015394]

21. Kern KA. Sentinel lymph node mapping in breast cancer using subareolar injection of blue dye. Journal of the American College of Surgeons. 1999; 189:539–545. [PubMed: 10589589]

22. Brader P, et al. Imaging of lymph node micrometastases using an oncolytic herpes virus and [F]FEAU PET. PloS one. 2009; 4:e4789. [PubMed: 19274083]

23. Tafreshi NK, et al. Noninvasive detection of breast cancer lymph node metastasis using carbonic anhydrases IX and XII targeted imaging probes. Clinical cancer research : an official journal of the American Association for Cancer Research. 2012; 18:207–219. [PubMed: 22016510]

24. Tafreshi NK, et al. A mammaglobin-A targeting agent for noninvasive detection of breast cancer metastasis in lymph nodes. Cancer research. 2011; 71:1050–1059. [PubMed: 21169406]

25. Savariar EN, et al. Real-time in vivo molecular detection of primary tumors and metastases with ratiometric activatable cell-penetrating peptides. Cancer research. 2013; 73:855–864. [PubMed: 23188503]

26. Weaver DL. Pathology evaluation of sentinel lymph nodes in breast cancer: protocol recommendations and rationale. Mod Pathol. 2010; 23 (Suppl 2):S26–32. [PubMed: 20436499]

27. Sexton K, et al. Pulsed-light imaging for fluorescence guided surgery under normal room lighting. Optics letters. 2013; 38:3249–3252. [PubMed: 23988926]

28. Porter CJ, Charman SA. Lymphatic transport of proteins after subcutaneous administration. Journal of pharmaceutical sciences. 2000; 89:297–310. [PubMed: 10707011]

29. Gerlinger M, et al. Intratumor heterogeneity and branched evolution revealed by multiregion sequencing. The New England journal of medicine. 2012; 366:883–892. [PubMed: 22397650]

30. Hettiarachchi K, Kim H, Faris GW. Optical manipulation and control of real-time PCR in cell encapsulating microdroplets by IR laser. Microfluidics and Nanofluidics. 2012; 13:967–975.

31. Liebert A, et al. Time-resolved multidistance near-infrared spectroscopy of the adult head: intracerebral and extracerebral absorption changes from moments of distribution of times of flight of photons. Applied optics. 2004; 43:3037–3047. [PubMed: 15176190]

32. Zhu Q, et al. Benign versus malignant breast masses: optical differentiation with US-guided optical imaging reconstruction. Radiology. 2005; 237:57–66. [PubMed: 16183924]

33. Flynn BP, Dsouza AV, Kanick SC, Davis SC, Pogue BW. White light-informed optical properties improve ultrasound-guided fluorescence tomography of photoactive protoporphyrin IX. Journal of biomedical optics. 2013; 18:46008.

34. Koral KF, et al. SPECT dual-energy-window Compton correction: scatter multiplier required for quantification. Journal of nuclear medicine : official publication, Society of Nuclear Medicine. 1990; 31:90–98.

35. Jenkins DE, Hornig YS, Oei Y, Dusich J, Purchio T. Bioluminescent human breast cancer cell lines that permit rapid and sensitive in vivo detection of mammary tumors and multiple metastases in immune deficient mice. Breast Cancer Res. 2005; 7:R444–454. [PubMed: 15987449]

36. Contag CH, Jenkins D, Contag PR, Negrin RS. Use of reporter genes for optical measurements of neoplastic disease in vivo. Neoplasia. 2000; 2:41–52. [PubMed: 10933067]

37. Reilly RM, et al. A comparison of EGF and MAb 528 labeled with 111In for imaging human breast cancer. Journal of nuclear medicine : official publication, Society of Nuclear Medicine. 2000; 41:903–911.

38. Peng X, et al. Phthalocyanine dye as an extremely photostable and highly fluorescent near-infrared labeling agent. Proc SPIE. 2006; 6097:19.

39. Wu F, et al. Fluorescence imaging of the lymph node uptake of proteins in mice after subcutaneous injection: molecular weight dependence. Pharmaceutical research. 2012; 29:1843–1853. [PubMed: 22373666]

40. Alcoser SY, et al. Real-time PCR-based assay to quantify the relative amount of human and mouse tissue present in tumor xenografts. BMC biotechnology. 2011; 11:124. [PubMed: 22176647]

41. Becker M, et al. Sensitive PCR method for the detection and real-time quantification of human cells in xenotransplantation systems. British journal of cancer. 2002; 87:1328–1335. [PubMed: 12439725]

42. Hamzei N, et al. Comparison of Kinetic Models for Dual-Tracer Receptor Concentration Imaging in Tumors. Austin J Biomed Eng. 2014; 1:9.

43. Samkoe KS, et al. High vascular delivery of EGF, but low receptor binding rate is observed in AsPC-1 tumors as compared to normal pancreas. Molecular imaging and biology : MIB : the official publication of the Academy of Molecular Imaging. 2012; 14:472–479. [PubMed: 21847690]

44. Tichauer KM, et al. Tumor endothelial marker imaging in melanomas using dual-tracer fluorescence molecular imaging. Molecular imaging and biology : MIB : the official publication of the Academy of Molecular Imaging. 2014; 16:372–382. [PubMed: 24217944]

45. Tichauer KM, et al. Accounting for pharmacokinetic differences in dual-tracer receptor density imaging. Physics in medicine and biology. 2014; 59:2341–2351. [PubMed: 24743262]

46. Tichauer KM, Samkoe KS, Klubben WS, Hasan T, Pogue BW. Advantages of a dual-tracer model over reference tissue models for binding potential measurement in tumors. Physics in medicine and biology. 2012; 57:6647–6659. [PubMed: 23022732]

47. Tichauer KM, et al. Improved tumor contrast achieved by single time point dual-reporter fluorescence imaging. Journal of biomedical optics. 2012; 17:066001. [PubMed: 22734757]

48. Lammertsma AA, Hume SP. Simplified reference tissue model for PET receptor studies. NeuroImage. 1996; 4:153–158. [PubMed: 9345505]

49. Innis RB, et al. Consensus nomenclature for in vivo imaging of reversibly binding radioligands. Journal of cerebral blood flow and metabolism : official journal of the International Society of Cerebral Blood Flow and Metabolism. 2007; 27:1533–1539.

50. Jacques SL. Optical properties of biological tissues: a review. Physics in medicine and biology. 2013; 58:R37–61. [PubMed: 23666068]

51. Ichise M, et al. Linearized reference tissue parametric imaging methods: application to [11C]DASB positron emission tomography studies of the serotonin transporter in human brain. Journal of cerebral blood flow and metabolism : official journal of the International Society of Cerebral Blood Flow and Metabolism. 2003; 23:1096–1112.

52. Lammertsma AA, et al. Comparison of methods for analysis of clinical [11C]raclopride studies. Journal of cerebral blood flow and metabolism : official journal of the International Society of Cerebral Blood Flow and Metabolism. 1996; 16:42–52.

53. Kety SS. The theory and applications of the exchange of inert gas at the lungs and tissues. Pharmacological reviews. 1951; 3:1–41. [PubMed: 14833874]

54. Patel D, et al. Monoclonal antibody cetuximab binds to and down-regulates constitutively activated epidermal growth factor receptor vIII on the cell surface. Anticancer research. 2007; 27:3355–3366. [PubMed: 17970081]
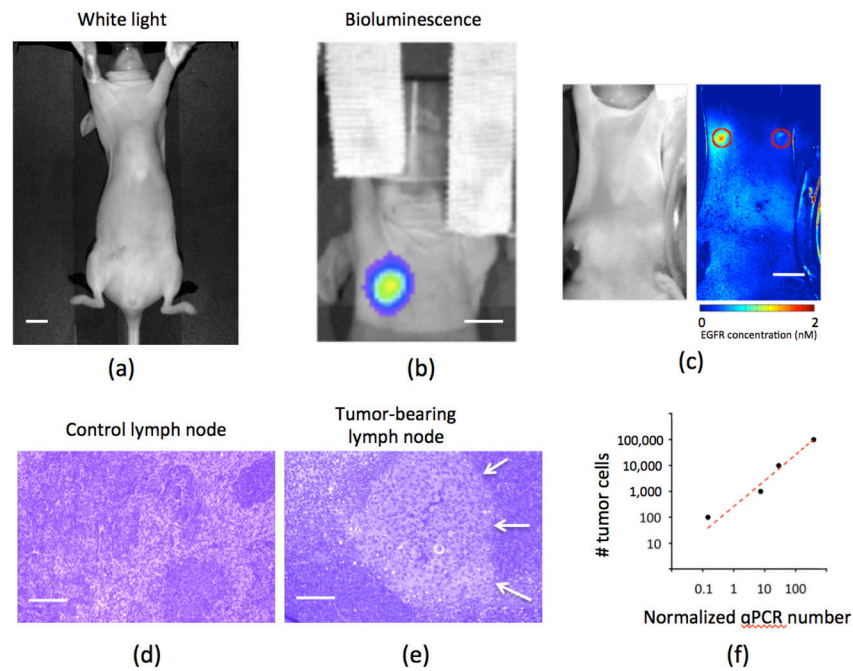
Figure 1. Animal model

A white-light image of a mouse positioned for axillary lymph node imaging is presented in (**a**) – (*n* = 1 of 22 mice imaged: 18 tumor bearing, 4 controls). A bioluminescence image demonstrating metastasis of cancer cells to the axillary lymph node using the MDA-MB-231-luc-D3H2LN cell line is demonstrated in (**b**). White light (left) and EGFR receptor concentration (right) images depicting typical regions of interest used for calculating the average EGFR concentration in a lymph node are presented in (**c**). Hemotoxylin and eosin stains of lymph node tissue from a healthy (left) and tumor-bearing mouse (right) are presented in (**d**) and (**e**) respectively. The white arrows are meant to locate a tumor cell cluster in (**e**). A standard curve relating quantitative PCR (qPCR) numbers to the number of tumor cells is presented in (**f**). The slope of this line was 257 tumor cells PCR#$^{-1}$. Scale bars are 1 cm in (**a**)-(**c**), and 500 μm in (**d**) and (**e**).
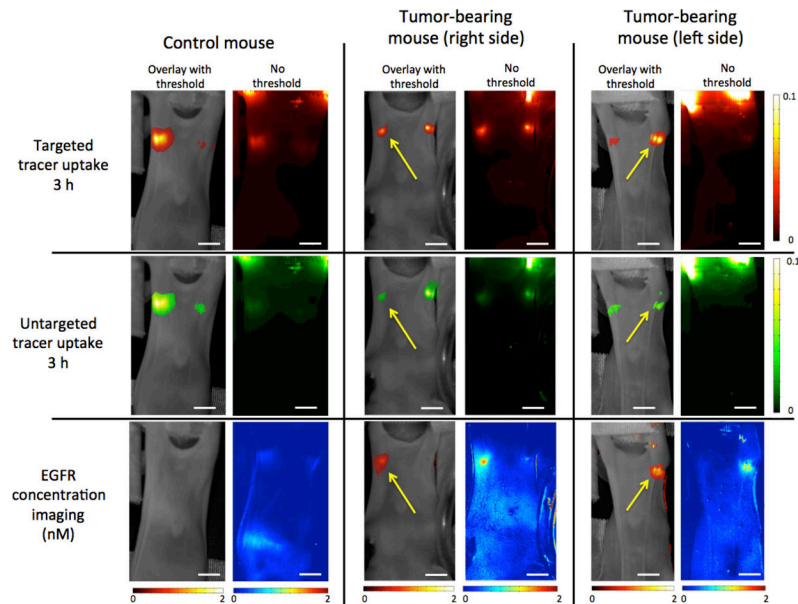
Figure 2. Lymph node molecular concentration imaging (LN-MCI)

A table of images with 3 rows and 3 columns is presented. In each table-cell there are two images: the left image is a white light image of a mouse with 30%-threshold overlays of the 3-hour post-injection signal from targeted fluorescence (top row of images), the 3-hour post-injection signal from untargeted fluorescence (middle row), or the EGFR concentration map (bottom row). Fluorescence from the injection sites of on the forelegs of the mice was also removed in the overlay images. The image on the right of each cell of the table corresponds to the corresponding fluorescence of EGFR concentration image alone with no thresholds. Each column corresponds to images from a representative mouse from the study: the first column of images pertain to a control mouse ($n = 1$ of 4 in the imaging study), the middle column of images pertain to a tumor-bearing mouse with verified tumor burden in the right axillary lymph node, and the last column of images pertain to a tumor-bearing mouse with verified tumor burden in the left axillary lymph node, where the yellow arrows denote the side with confirmed tumor burden ($n = 2$ tumor-bearing mice of 18 included in the imaging study). The units of fluorescence are in percent of the dynamic range of the Pearl Imaging System (*i.e.*, a unit of 100 would be the level of saturation), and the units of the EGFR concentration maps are in nM. Scale bars are 1 cm.
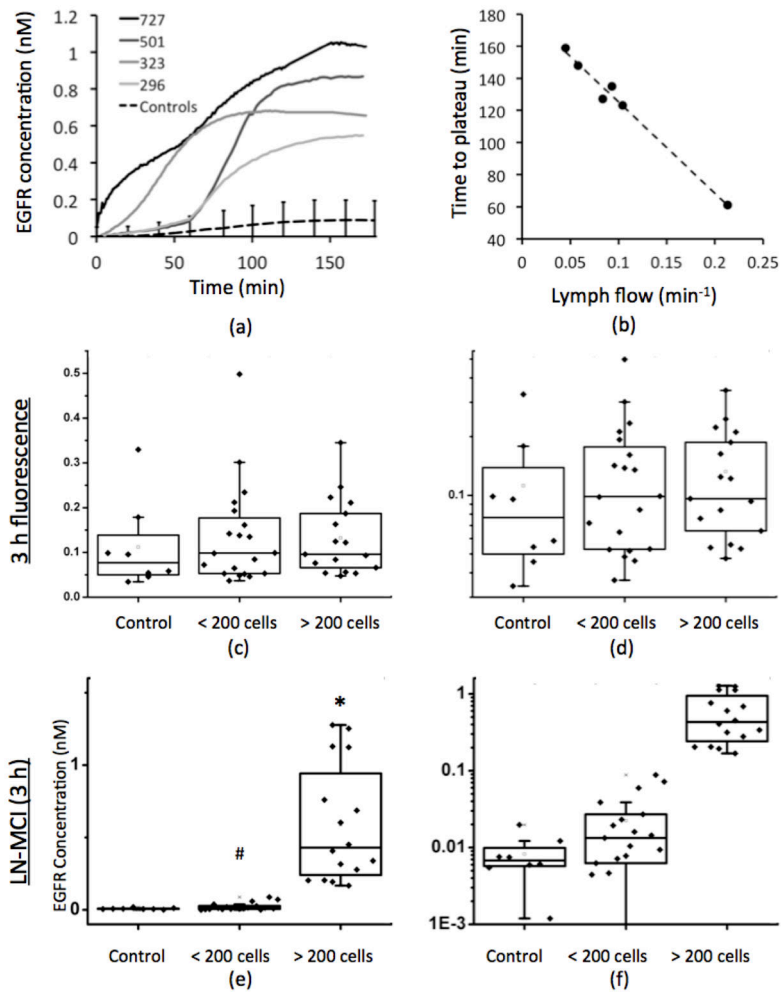
Figure 3. Dual-tracer compared to single tracer imaging

Ratiometric estimations of EGFR concentration [(targeted – untargeted)/untargeted] as a function of time after tracer injection are presented in (**a**) for lymph nodes with various levels of tumor burden determined by quantitative PCR (black = 727 cells, dark gray = 501 cells, gray = 323 cells, and light gray = 296 cells (n = 4 lymph nodes of 36 imaged); and dashed black = mean ± s.d. of 8 lymph nodes from 4 control mice). A correlation between the time to plateau of the curves in (**a**) and the average lymph flow rates for all tumor bearing lymph nodes is presented in (**b**). The dashed line represents the linear regression of the data. Average fluorescence signal measured from the uptake of the EGFR targeted tracer at 3 h post-injection in the axillary lymph nodes of control mice (n = 4; 8 nodes), nodes from tumor-bearing mice with less than 200 tumor cells detected by qPCR (n = 10; 20 nodes), nodes from tumor-bearing mice with greater than 200 tumor cells detected by qPCR (n = 8, 16 nodes), are presented in a boxplot format in (**c**). The units of fluorescence correspond to percentage of the dynamic range of the CCD camera used to detect the fluorescence in the Pearl Imaging System. The same boxplot format is used to compare the average EGFR concentrations measured *in vivo* in each lymph node using the single time point lymph node receptor imaging (LN-MCI) model in (**e**). *$p < 0.001$ compared to control and < 200 cell

groups. $^{\#}p < 0.05$ compared to the control group using a one-tailed t-test and Tamhane correction for multiple comparisons with unequal variance. Groups in the LN-MCI plots were non-normal by Shapiro-Wilk Test so Kruskal-Wallis nonparametric test was used to determine significance rather than one-way ANOVA. Logscale plots of (**c**) and (**e**) are presented in (**d**) and (**f**), respectively, to illuminate group differences. Errobars are s.d..
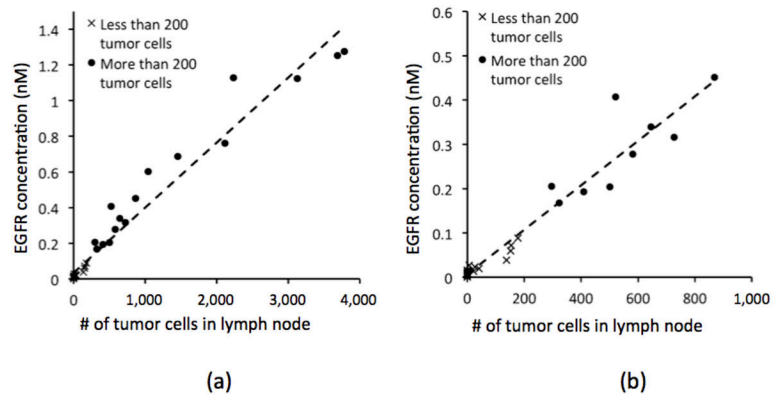
Figure 4. Estimation of tumor burden

The correlation between dual-tracer imaging estimates of axillary lymph node tumor burden at 3 h post-tracer injection and qPCR tumor burden measures is presented in (**a**): $n = 36$ axillary lymph nodes from 18 mice. The blue circles represent data from lymph nodes with greater than 200 tumor cells detected by qPCR and the red exes represent those with less than 200 tumor cells detected. The plot in (**b**) is the same as in (**a**) but for lymph nodes with less than 1,000 cells to provide a clearer view of the correlation at lower tumor burden. Linear regression (dashed black lines) determined the correlation in (**a**) and (**b**) to be statistically significant (slope: 0.4 pM cell^{-1} cm^{-2} $r = 0.97$, $p < 0.01$ in both plots).
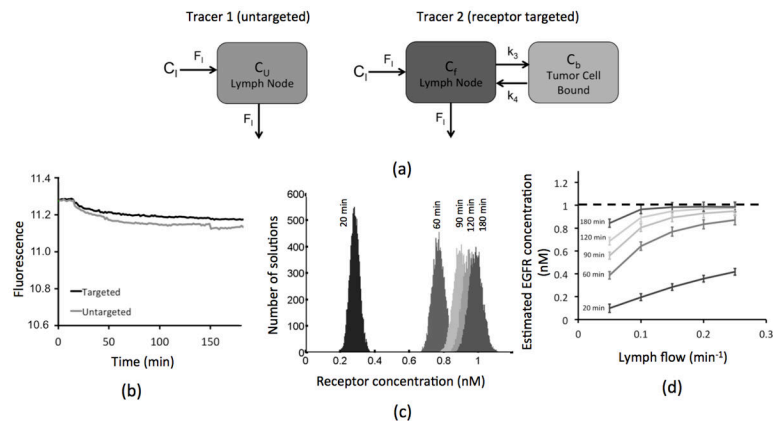
Figure 5. Modeling and simulations

The tracer kinetic compartment model for the targeted (right side) and the untargeted (left side) tracers is depicted in (**a**). C_l represents the concentration of tracer in the upstream lymph vessels feeding the sentinel lymph node, C_U represents the concentration of untargeted tracer in the lymph node, C_f represents the concentration of unbound targeted tracer in the lymph node, C_b represents the concentration of specifically bound targeted tracer in the lymph node, F_l represents the lymph fluid flow rate, and k_3 and k_4 represent the rates of association and dissociation, respectively, of the targeted tracer with its receptor. Typical curves of average fluorescence at the site of injection for the targeted tracer (red curve) and the untargeted tracer (green curve) are plotted in (**b**). The results of a simulation study noise analysis are presented in the form of a histogram in (**c**), with applying the single-time-point receptor concentration estimate at 20, 60, 120, and 180 min after tracer injection for a lymph flow rate of 0.15 min^{-1} and a simulated receptor concentration of 1 nM. The mean ± s.d. of the histograms plotted in (**c**) are depicted in (**d**) for over a range of theoretical lymph flow rates.